High-Performance Sodium Ion Batteries Based on a 3D Anode from Nitrogen-Doped Graphene Foams

Jiantie Xu, Min Wang, Nilantha P. Wickramaratne, Mietek Jaroniec, Shixue Dou, and Liming Dai**

Over the past several decades, lithium ion batteries (LIBs) have been successfully used as the rechargeable energy source of choice in various portable and smart devices (e.g., personal computers, cell phones, cameras, MP3 players) because of their high energy density and long lifetime.[1] A continuously growing demand for them in large-scale applications, such as electric vehicles (EVs) and hybrid electric vehicles (HEVs), raises great concerns about the high cost ($5000/ton for lithium) and limited terrestrial reservation of lithium.[2] Therefore, sodium ion batteries (SIBs), based on the earth-abundant inexpensive sodium ($150/ton for sodium) from the alkaline family, have recently attracted increasing attention as a low-cost alternative to LIBs. So far, there are a few anode materials have been identified for SIBs while a large number of potential cathode materials, including $NaCrO_2$, $Na_{0.44}MnO_2$, NaV_6O_{15}, $NaNi_{1/3}Mn_{1/3}Fe_{1/3}O_2$, $Na_{2/3}[M_xMn_{1-x}]O_2$, $NaMF_3$ (M = Fe, Mn, V, and Ni), $NaFePO_4$, Na_2MPO_4F, and $Na_3M_2(PO_4)_3$ (M = Fe, Mn, Co, and Ni), were developed.[2a,3] Consequently, one of the major critical issues for the development of high-performance SIBs is to identify suitable anode materials. Being earth-abundant, cost-effective, eco-friendly, thermally stable, and electrically conductive, carbon nanomaterials are considered to be one of the most promising candidates among the limited number of various anode materials for SIBs, including $Na_2Ti_3O_7$, $NiCo_2O_4$, TiO_2, Sn, P/C, and $Li_4Ti_5O_{12}$.[2–4] Nevertheless, the commonly-used commercial graphite anode has been demonstrated to show a low reversible capacity in SIBs (Table S1, Supporting Information).[5] On the other hand, a variety of other carbon based materials (Table S1, Supporting Information), such as hard carbon,[6] carbon black,[7] cellulose and polyparaphenylene,[8] petroleum coke,[9] carbon spheres,[10] porous carbon,[11] carbon fibers,[12] carbon nanotubes,[13] and graphene,[14] were found to facilitate the insertion/extraction of sodium ions into/from the host structures of SIBs. Recent research results indicate that the improvement of the electrochemical performance of SIBs strongly depend on the morphology and pore size of carbon materials at anodes.[6,10–14] Furthermore, heteroatom doping (e.g., N, B, S, and P) of carbon nanomaterials, including graphene, has been demonstrated to significantly enhance the electrical conductivity and surface hydrophilicity of carbon-based electrodes to facilitate the charge transfer and electrode–electrolyte interactions.[15] In this regard, N-doped carbon nanomaterials have been explored as the anode materials for LIBs and SIBs.[16,11b,11c,12a,12c] Examples include LIBs based on anodes from N-doped (3.06 at% nitrogen) graphene (a reversible capacity of >1040 mAh g^{-1} at a current density of 50 mA g^{-1} in the voltage range of 0–2 V),[16a] N-doped porous carbon nanofibers (a capacity of ≈152 mAh g^{-1} with 88.6% capacity retention after 200 cycles at 200 mA g^{-1} in the voltage range of 0–2 V),[11b] and N-doped porous carbon sheets (a highly reversible capacity of 349.7 $mAhg^{-1}$ with ≈50% capacity retention after 260 cycles at 50 mA g^{-1} in the voltage range of 0–3 V).[12a] The performance of other SIBs based on carbon anodes is summarized in Table S1 (Supporting Information). As can be seen, the carbon-based anodes in SIBs still suffer from a much lower capacity and rate capability with respect to LIB counterparts.

As mentioned above, the morphology and pore size of carbon anodes play important roles in regulating the Na^+ transport and storage in SIBs.[6,10–14] The use of carbon nanomaterials with a well-defined 3D morphology and pore size, in conjunction with heteroatom-doping, could lead to ideal anodes for SIBs with high performance. However, the potential use of 3D nanocarbon anodes for SIBs has hardly been investigated, though various 3D carbon electrodes with excellent charge/ion transport and mechanical properties in all dimensions have found applications in solar cells,[17] supercapacitors,[18] fuel cells,[19] and even LIBs.[20] In the present study, we prepared 3D N-doped graphene foams (N-GF) (Product 6 in Figure S1, Supporting Information) with a high 6.8 at% nitrogen content (elemental analysis shown in Table S2, Supporting Information) by annealing the freeze-dried graphene oxide foams (GOF) (Product 3, Figure S1, Supporting Information) in ammonia,[17] and used them as the anode for SIBs. The use of the GOF (Product 3, Figure S1, Supporting Information) as a precursor for the post-synthesis annealing in ammonia allowed for a low-cost, large-scale production of 3D N-GF.[17] For comparison, we have also prepared reduced graphene (rG) (1 → 2), nitrogen-doped graphene (N-G) (1 → 4), and reduced graphene

Dr. J. Xu, M. Wang, Prof. L. Dai
Department of Macromolecular Science and Engineering
Case Western Reserve University
Cleveland, OH 44106, USA
E-mail: liming.dai@case.edu
Dr. J. Xu, Prof. S. Dou
Institute for Superconducting and Electronic Materials
University of Wollongong
Wollongong, NSW 2522, Australia
E-mail: shi_dou@uow.edu.au
Dr. N. P. Wickramaratne, Prof. M. Jaroniec
Department of Chemistry and Biochemistry
Kent State University
Kent, OH 44242, USA

DOI: 10.1002/adma.201405370

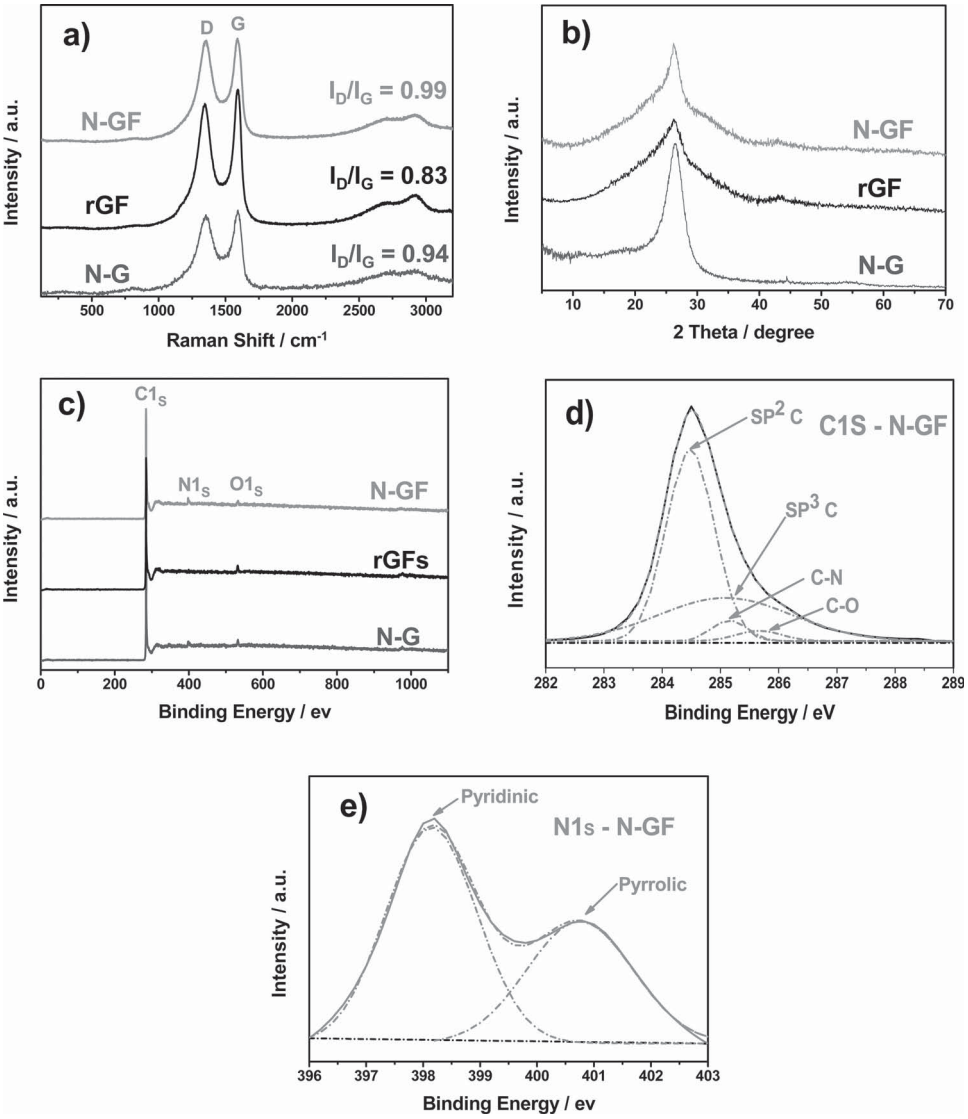

Figure 1. a) Raman spectra and b) XRD patterns of the N-G, rGF, and N-GF. c) X-ray photoelectron survey spectra (XPS) of the N-G, rGF, and N-GF. d) High-resolution XPS C1s spectrum of N-GF and e) high-resolution XPS N1s spectrum of the N-GF.

foams (rGF) (1 → 3 → 5) (Figure S1, Supporting Information, for experimental details).

Figure 1a shows Raman spectra of the N-G, rGF, and N-GF, all of which revealed the pronounced D and G bands at around 1349 cm^{-1} and 1592 cm^{-1}, respectively. The N-GF sample exhibited the highest peak intensity ratio of the D to G band (I_D/I_G = 0.99) as compared to the corresponding ratios for the N-G (I_D/I_G = 0.94) and rGF (I_D/I_G = 0.83) because of the structural distortion induced by N-doping and the edge defects associated with the 3D foam-like structure. Both the N-doping and edge defects could enhance the electrocatalytic activity of the N-GF electrode.[17,21] X-ray diffraction (XRD) profiles for N-G, rGF, and N-GF are shown in Figure 1b. As can be seen, a characteristic (002) peak for graphitic carbon appeared at 26.1°, 26.1°, and 26.0° for the N-G, rGF, and N-GF, corresponding to a layer-to-layer distance (*d*-spacing) of 0.341, 0.341, and 0.342 nm, respectively. Compared to a d-spacing of 0.336 nm for conventional graphite, the observed larger *d*-spacing for the N-G, rGF, and N-GF samples is important for the insertion/extraction of relatively large sodium ions.[22] Figure 1c displays the X-ray photoelectron spectroscopic (XPS) survey spectra of the N-G, rGF, and N-GF, which show a pronounced XPS C1s peak at about 285 eV for all of the three samples, along with a much weaker O 1s peak at 534 eV (2.8 at% for N-G, 3.2 at% for rGF, and 2.7 at% for N-GF). Upon doping with nitrogen to produce the N-G (5.4 at%) and N-GF (5.9 at%), the N1s peak appeared at about 400 eV (Figure 1c). High-resolution XPS C1s spectra of the rGF, N-G, and N-GF are presented in Figures S2b–d (Supporting Information), respectively (Figure 1d). These C1s XPS peaks can be deconvoluted into a dominated component for sp^2-C at 284.5 eV, along with other weaker bands associated with sp^3-C at 285.4 eV, C–N at 285.2 eV, and C–O at 285.9 eV, respectively.[23] As shown in Figure 1e and Figure S2f d), the high resolution XPS N1s spectra of the

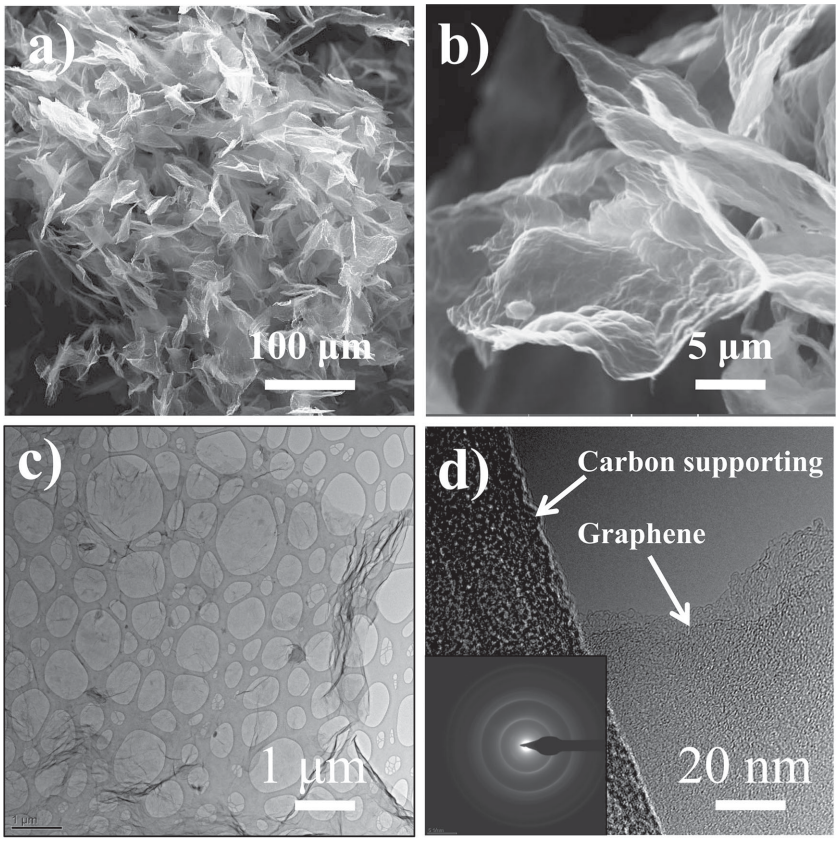

Figure 2. a,b) SEM images and c,d) STEM images of the N-GF. Inset of (d) is the SAED pattern of the N-GF.

N-GF and N-G can be deconvoluted into two peaks at 398.2 and 400.6 eV corresponding to the pyridinic nitrogen and pyrrolic nitrogen, respectively.[17,24]

To examine the morphology of the materials studied, we performed scanning electron microscopy (SEM) and transmission electron microscopy (TEM) imaging. SEM images of the rG (Figure S3a, Supporting Information) and N-G (Figure S3b, Supporting Information) show mainly the "plate-like" graphene. By contrast, all of the foam samples, including the GOF (Figure S3c, Supporting Information), rGF (Figure S3d, Supporting Information), and N-GF (Figure S3e, Supporting Information, **Figure 2**a,b), exhibit a foam-like surface structure consisting of "flake-like" graphene sheets. A comparison of the higher magnification SEM image of the rG (Figure S3a2, Supporting Information) with that of rGF (Figure S3d2, Supporting Information) indicates that the foam sample possesses a more loosely packed graphitic sheets. Similar morphology difference was observed between the N-G (Figure S3b2, Supporting Information) and N-GF (Figure S3e2, Supporting Information), which could lead to a higher sodium ion storage in the foam-like electrode during discharge/charge processes. Figure 2c,d and Figure S4 (Supporting Information) show the corresponding TEM images for the N-G, rGF, and N-GF. The low magnification TEM images in Figure S4a1–a3 (Supporting Information) show that the N-G, rGF, and N-GF were all composed of transparent thin films with some thicker ripples, indicating a single and/or few layered wrinkled graphene sheets. The corresponding high resolution TEM images in Figure S4b1–b3 (Supporting Information) show largely amorphous structures for the N-G, rGF, and N-GF, which are also indicated by the diffused rings seen in the associated selected area electron diffraction (SAED) patterns (Figure S4c1–c3, Supporting Information). It seems that the partial crystallization of the amorphous GO starting materials resulted in the formation of small crystalline domains (cf. Figure 1b) interdispersed in the amorphous matrix; the latter showed up dominantly in the TEM images. The partial crystallization of N-GF was further confirmed by HRTEM (Figure S4d, Supporting Information). As can be seen, an estimated lattice spacing of 0.347 nm (i.e., 1.04/3 nm) in the crystalline domain is consistent with the XRD results, both indicating that the lattice spacing of the N-GF is larger than that of conventional graphite, which is important for the insertion/extraction of relatively large sodium ions. Besides, the partially crystalline domains could enhance the charge transport and stabilize the foam-like amorphous carbon matrix during the discharge–charge process. The stable 3D matrix would provide additional sites for sodium storage without volume expansion, and hence enhanced storage capacity and cycling performance.[11d,12a,14,16e,16f]

Figure 3a reproduces the discharge/charge profiles for the N-G, rGF, and N-GF at 0.2 C in the voltage range of 0.02–3 V, which shows two apparent plateaus in the first discharge process for all of the three samples. Note that the second discharge plateau at around 0.1 V for the N-GF is longer as compared to those for the rGF and N-G within the first cycle, indicating a larger amount of sodium ions have inserted into the N-GF during the discharge process. This phenomenon was also confirmed by cyclic voltammetry (CV) measurements. As shown in Figure S5b,d,f (Supporting Information), a strong cathodic peak was observed for the N-G (C1), rGF (C3), and N-GF (C5) electrodes at around 0.7 V, corresponding to the first discharge plateaus in the first discharge curves shown in Figure 3a. These pronounced peaks were generated from the electrolyte decomposition, leading to the formation of the solid electrolyte interphase (SEI) films on the surfaces of the graphene electrodes. However, the intensity of the second cathodic peak of the N-GF electrode recorded at around 0.1 V (C6) was much higher than those recorded for the rGF (C4) and N-G (C2), which is consistent with the longer second discharge plateau seen in Figure 3a. The electrolyte decomposition for the SEI formation in our SIBs occurred at about 0.7 V, which is very close to the equivalent values for certain LIBs[16c,16d] and SIBs based on N-doped carbon nanofibers.[11b] In the subsequent discharge cycles, the cathodic peaks (C1, C3, and C5) for the N-G, rGF, and N-GF, respectively, disappeared (Figure S5b,d,f, Supporting Information) due to the presence of the dense SEI films formed during the first discharge cycle.

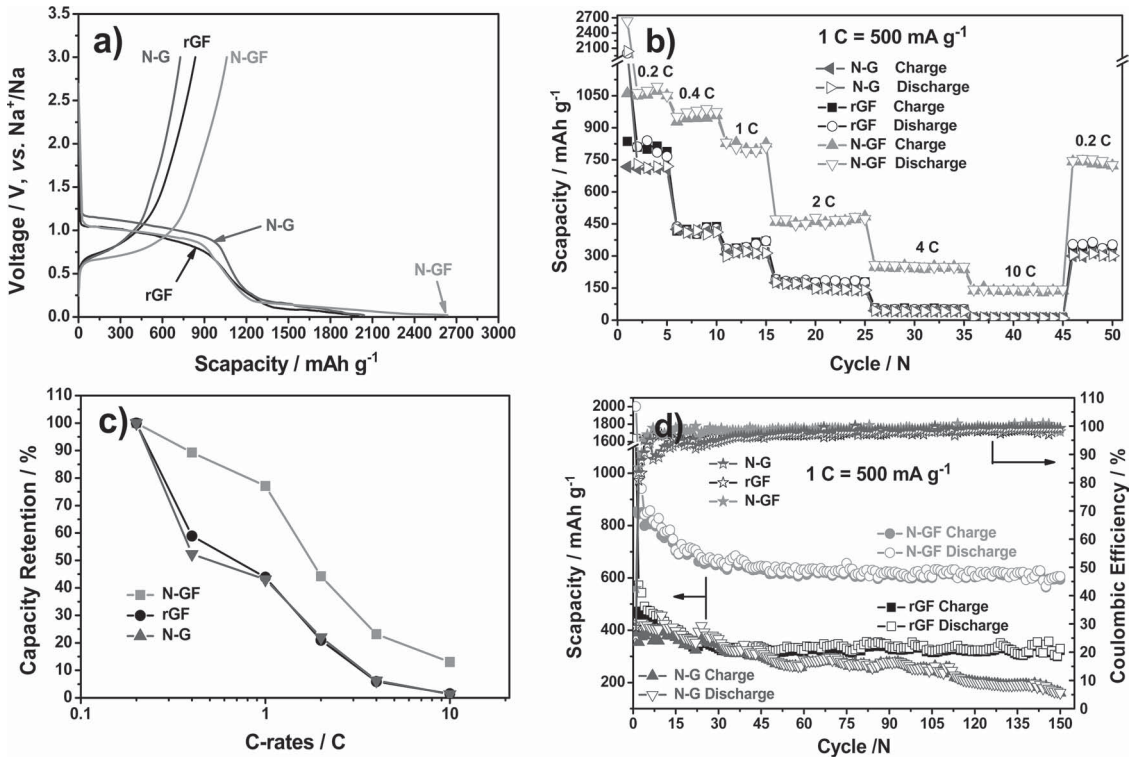

Figure 3. a) Initial charge–discharge curves of the N–G, rGF, and N–GF at 0.2 C; b) rate performance of the N-G, rGF, and N-GF from 0.2 C to 10 C; c) capacity retention of the initial capacity at 0.2 C versus C-rate; and d) cycling performance of the N-G, rGF, and N-GF at 1 C in the voltage range of 0.02–3.0 V (assumed 1 C = 500 mA g^{-1}; Scapacity = specific capacity).

During the charge process, however, the two anodic peaks (A5 and A6) at around 0.97 and 0.75 V for the N-GF became stronger during the subsequent cycles (Figure S5f, Supporting Information), whereas the relatively weak anodic peaks (A3 and A4) for the rGF (Figure S5d, Supporting Information) and (A1 and A2) for the N-G (Figure S5b, Supporting Information) further weakened to disappear in the following cycles. The presence of pronounced and highly overlapped anodic peaks could be attributed to the partial oxidation of Na-OX groups, which are generated from the interaction between sodium ions and oxygen containing functional groups during the discharge process. Therefore, the more highly reversible Na-OX redox reactions for N-GF than N-G and rGF indicate that the N-GF anode has a higher sodium ion insertion/extraction capability than the rGF and N-G in the SIBs.

To test the rate and cycling performance, we charged and discharged SIB cells based on the N-G, rGF, and N-GF anodes for 50 cycles in the voltage range of 0.02–3 V from 0.2 to 10 C (Figure 3b, Supporting Information). As shown in Figure S6d (Supporting Information), the initial reversible capacities of the N-G and rGF are 717.4 and 836.2 mAh g^{-1} at 0.2 C, which are about 1.77 and 2.06 times that of the r-G (406.2 mAh g^{-1}), respectively, and much higher than that of the GOF with 18.7 mAh g^{-1} (Figure S6b, Supporting Information). When the C rate was increased from 0.2 to 1 C, the N-G and rGF both still showed higher reversible capacity than that of the r-G (Figure S6d, Supporting Information). Thus, either the foam-like structure or N-doping could significantly improve the electrochemical performance. As expected, therefore, the N-GF exhibited much higher average charge capacities of 1057.1 (0.2 C), 943.5 (0.4 C), 815.2 (1 C), 467.1 (2 C), 244.7 (4 C), and 137.7 (10 C) mAh g^{-1} than those of 707.4 (0.2 C), 416.4 (0.4 C), 310.2 (1 C), 148.2 (2 C), 41.8 (4 C), and 10.3 (10 C) mAh g^{-1} for the N-G, and 809.4 (0.2 C), 423.3 (0.4 C), 348.7 (1 C), 178.3 (2 C), 51.0 (4 C), and 10.5 (10 C) mAh g^{-1} for the rGF (Figure 3b). As shown in Figure 3c, the charge capacity retention after 45 cycles at 10 C for N-GF (13%) was also higher than those for the NG (1.5%) and rGF (1.3%).

Figure 3d shows the relatively long-term cycling performance for the N-G, rGF, and N-GF measured at 1 C in the voltage range of 0.02–3 V. As can be seen, the N-G, rGF, and N-GF exhibited the initial discharge/charge capacities of 1550.0/391.1, 1636.9/472.3, and 2000.5/852.6 mAh g^{-1} with an initial Coulombic efficiency of 25.6%, 28.8%, and 42.6%, respectively. The large capacity loss of the initial discharge/charge capacities is mainly attributed to the reductive decomposition of the electrolyte and the formation of a dense SEI film due to the large surface area, and irreversible reaction between sodium ions and the residual oxygen-containing functional group of the graphene.[10b,12a,12f,14b] After 150 cycles, the N-G, rGF, and N-GF cells can deliver discharge/charge capacities of 161.1/160.1, 329.6/323.1, and 605.6/594.0 mAh g^{-1} with the initial capacity retention of 10.4%/40.9%, 20.1%/68.4%, and 30.3%/69.7%, respectively. In spite of the relatively low Coulombic efficiencies for the N-G, rGF, and N-GF in the first cycle, all electrodes exhibited a much higher average Coulombic efficiency of 97.9% for the N-G, 97.2% for the rGF, and 98.9% for the N-GF over 150 cycles. The higher discharge/charge capacities, capacity

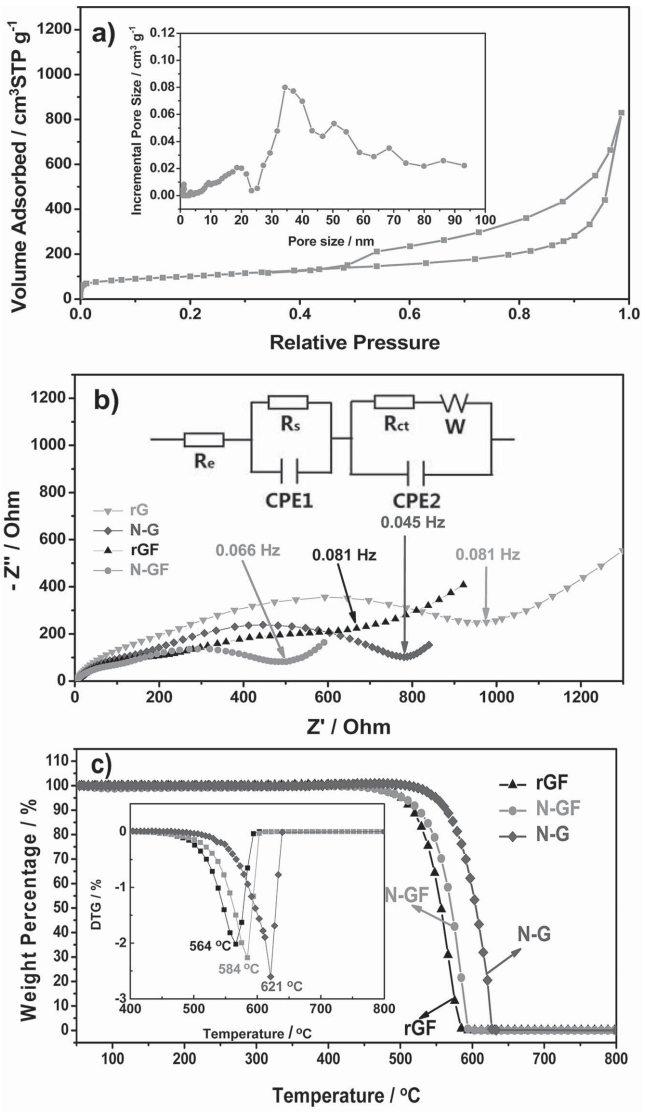

Figure 4. a) Nitrogen adsorption–desorption isotherm and the corresponding DFT incremental pore size distribution curve (inset in Figure 4a) for the N-GF; b) impedance plots and equivalent circuit (inset) used for the EIS analysis of the rG, N-G, rGF, and N-GF; and c) thermogravimetric (TG) and differential thermogravimetric (DTG) profiles (inset) of the N-G, rGF, and N-GF.

retention, and Coulombic efficiency observed for the N-GF than those of the N-G and rGF indicate, once again, that the N-GF anode has a better cycling performance with respect to the N-G and rGF electrodes. Moreover, as shown in Figure S7 (Supporting Information), the N-GF cell also exhibited a lower electrode polarization (≈65% capacity secured under 1.0 V over 150 cycles) than those of the N-G and rGF.

To gain a better understanding of the observed superb electrochemical performance for the N-GF, nitrogen adsorption studies were performed. As shown in **Figure 4**a and Figure S8a1–d1 (Supporting Information), all adsorption isotherms for the rG, N-G, rGF, and N-GF show small hysteresis loops over the relative pressure range of 0.50–0.95. Insets in Figure 4a and Figure S8a2–d2 (Supporting Information) show the incremental pore size distributions calculated from the corresponding adsorption isotherms by using the density functional theory (DFT) method for slit-like pore geometry. These distributions indicate the presence of abundant mesopores (≈40 nm) in the samples. The BET specific surface areas for the rG, N-G, rGF, and N-GF samples are listed in Table S3 (Supporting Information), which shows the highest surface area of 357 m^2 g^{-1} for the N-GF. The large surface area, together with the 3D mesoporous structure and N-doping-induced defects, makes the 3D N-GF favorable for the fast diffusion of the relatively large-sized sodium ions with a low ion-transport resistance and effective storage of sodium ions during discharge–charge processes.[11,16] Figure S9 (Supporting Information) shows the electrochemical impedance spectra (EIS) for the rG, N-G, rGF, and N-GF measured before cycling and after 3 cycles (Figure 4b). The Nyquist plot for each of the cells shows a semicircle with a large diameter at high frequencies before cycling. Upon cycling, the depressed two semicircles at high frequencies and medium frequencies suggest a new impedance formation and a decreased impedance after cycling due to the SEI formation and electrode/electrolyte activation. The kinetic parameters obtained from the equivalent circuit fitting are listed in Table S4 (Supporting Information). As can be seen in Table S4 (Supporting Information), the charge-transfer resistances (R_{ct}) calculated by using the equivalent circuit model (Figure 4b) for all the samples are decreased after 3 discharge–charge cycles, attributable to the electrode–electrolyte activation in the initial cycles. Meanwhile, the R_{ct} for all of the samples decreased in the same order before and after cycling, as exemplified by the order of rG (839.8 Ω), N-G (744.8 Ω), rGF (604.1 Ω), and N-GF (502.0 Ω) after 3 cycles, indicating the highest ionic conductivity for the N-GF.

As shown in Figure 4c, our thermogravimetric analyses (TGA) and differential thermogravimetry (DTG) profiles further indicate that N-doping enhanced thermal stability of the N-GF and N-G, as exemplified by an increase in the decompression temperature from 564 °C for rGF to 584 °C for N-GF and 621 °C for N-G, probably due to the doping-induced reduction process.[16a] The relatively low decomposition temperature for the N-GF (584 °C) with respect to that of the N-G (621 °C) suggests that the 3D graphene foam with a high surface area (Table S3, Supporting Information) in the N-GF sample is more susceptible to thermal decomposition. However, the "foam-like" 3D structure could act as a buffer to alleviate the volume expansion associated with excessive sodium intercalation, and hence improve the cycling life,[11d,12a,16e,16f] leading to an overall high performance for the N-GF-based SIBs. Furthermore, as shown in Figure S10 (Supporting Information), the ex situ XRD of the N-GF electrode at different discharge voltages of 2.8 V (open circuit voltage), 0.9 V (SEI formation), 0.02 V (full discharge) indicated various degrees of sodiation in the graphene throughout the discharge process. In the charge process, there is no obvious XRD peak shift for the N-GF at 1.0 V with a complete amorphous feature at 3.0 V (full charge) without any distinct peaks, indicating a stable structure of the N-GF with an estimated volumetric capacity of 220 mAh cm^{-3} (Figure S11, Supporting Information).

In summary, we have demonstrated, for the first time, that 3D N-GF can be used as anode to significantly improve the

overall performance of SIBs. Specifically, we found that the 3D N-GF delivered an unusually high initial reversible capacity of 852.6 mAh g^{-1} at a current density of 1 C (1 C = 500 mA g^{-1}) between 0.02 and 3 V. After 150 cycles, the N-GF could still maintain a charge capacity of 594 mAh g^{-1} with 69.7% retention of the initial charge capacity, significantly outperformed previously reported carbonaceous materials (Table S1, Supporting Information). The observed superb performance of the 3D N-GF anode in SIBs was attributed to synergistic effects associated with the 3D mesoporous structure with a well-defined porosity, large surface area, and enlarged lattice spacing between grapheme layers, coupled with the N-doping-induced defects, to facilitate the diffusion of the large-size sodium ions, enhance the storage of sodium ions, and minimize the effect of volume expansion during discharge–charge processes. This work clearly indicates that 3D carbon nanomaterials with well-defined structures and heteroatom-doping induced defects could be used as anode materials for the development of high-performance sodium ion batteries and other energy devices.

Supporting Information

Supporting Information is available from the Wiley Online Library or from the author.

Acknowledgements

The authors are grateful for financial support from AFOSR (Grant Nos. FA9550–12–1–0037 and FA-9550–12–1–0069), NSF (Grant Nos. NSF-CMMI-1000768, NSF-CMMI-1400274, and NSF-DMR-1106160), and Auto CRC 2020. The authors thank Dr. T. Silver for critical reading of the manuscript.

Received: November 24, 2014
Revised: January 13, 2015
Published online: February 16, 2015

[1] J. B. Goodenough, K.-S. Park, *J. Am. Chem. Soc.* **2013**, *135*, 1167.
[2] a) M. D. Slater, D. Kim, E. Lee, C. S. Johnson, *Adv. Funct. Mater.* **2013**, *23*, 947; b) V. L. Chevrier, G. Ceder, *J. Electrochem. Soc.* **2011**, *158*, A1011.
[3] a) V. Palomares, P. Serras, I. Villaluenga, K. B. Hueso, J. Carretero-Gonzalez, T. Rojo, *Energy Environ. Sci.* **2012**, *5*, 5884; b) S. W. Kim, D. H. Seo, X. H. Ma, G. Ceder, K. Kang, *Adv. Energy Mater.* **2012**, *2*, 710; c) J. Xu, S.-L. Chou, J.-L. Wang, H.-K. Liu, S.-X. Dou, *ChemElectroChem* **2014**, *1*, 371; d) K. B. Hueso, M. Armand, T. Rojo, *Energy Environ. Sci.* **2013**, *6*, 734.
[4] Y. Sun, L. Zhao, H. Pan, X. Lu, L. Gu, Y.-S. Hu, H. Li, M. Armand, Y. Ikuhara, L. Chen, X. Huang, *Nat. Commun.* **2013**, *4*, 1870.
[5] a) P. Ge, M. Fouletier, *Solid State Ionics* **1988**, *28–30*(Part 2), 1172; b) M. M. Doeff, Y. P. Ma, S. J. Visco, L. C. Dejonghe, *J. Electrochem. Soc.* **1993**, *140*, L169.
[6] a) P. Thomas, J. Ghanbaja, D. Billaud, *Electrochim. Acta* **1999**, *45*, 423; b) D. A. Stevens, J. R. Dahn, *J. Electrochem. Soc.* **2001**, *148*, A803; c) D. A. Stevens, J. R. Dahn, *J. Electrochem. Soc.* **2000**, *147*, 1271; d) P. Thomas, D. Billaud, *Electrochim. Acta* **2002**, *47*, 3303; e) S. Komaba, W. Murata, T. Ishikawa, N. Yabuuchi, T. Ozeki, T. Nakayama, A. Ogata, K. Gotoh, K. Fujiwara, *Adv. Funct. Mater.* **2011**, *21*, 3859; f) A. Ponrouch, A. R. Goni, M. R. Palacin, *Electrochem. Commun.* **2013**, *27*, 85; g) X. Zhou, Y.-G. Guo, *Chem ElectroChem* **2014**, *1*, 83; h) A. Fukunaga, T. Nohira, R. Hagiwara, K. Numata, E. Itani, S. Sakai, K. Nitta, S. Inazawa, *J. Power Sources* **2014**, *246*, 387; i) C. Bommier, W. Luo, W.-Y. Gao, A. Greaney, S. Ma, X. Ji, *Carbon* **2014**, *76*, 165.
[7] R. Alcantara, J. M. Jimenez-Mateos, P. Lavela, J. L. Tirado, *Electrochem. Commun.* **2001**, *3*, 639.
[8] a) M. Dubois, A. Naji, D. Billaud, *Electrochim. Acta* **2001**, *46*, 4301; b) M. Dubois, D. Billaud, *Electrochim. Acta* **2002**, *47*, 4459.
[9] a) R. Alcantara, J. M. J. Mateos, J. L. Tirado, *J. Electrochem. Soc.* **2002**, *149*, A201; b) E. Zhecheva, R. Stoyanova, J. M. Jimenez-Mateos, R. Alcantara, P. Lavela, J. L. Tirado, *Carbon* **2002**, *40*, 230; c) R. Alcantara, P. Lavela, G. F. Ortiz, J. L. Tirado, R. Menendez, R. Santamaria, J. M. Jimenez-Mateos, *Carbon* **2003**, *41*, 3003.
[10] a) R. Alcántara, P. Lavela, G. F. Ortiz, J. L. Tirado, *Electrochem. Solid State Lett.* **2005**, *8*, A222; b) K. Tang, L. J. Fu, R. J. White, L. H. Yu, M. M. Titirici, M. Antonietti, J. Maier, *Adv. Energy Mater.* **2012**, *2*, 873; c) T. Chen, L. Pan, T. Lu, C. Fu, D. H. C. Chua, Z. Sun, *J. Mater. Chem. A* **2014**, *2*, 1263; d)V. G. Pol, E. Lee, D. Zhou, F. Dogan, J. M. Calderon-Moreno, C. S. Johnson, *Electrochim. Acta*, **2014**, *127*, 61.
[11] a) S. Wenzel, T. Hara, J. Janek, P. Adelhelm, *Energy Environ. Sci.* **2011**, *4*, 3342; b) Z. H. Wang, L. Qie, L. X. Yuan, W. X. Zhang, X. L. Hu, Y. H. Huang, *Carbon* **2013**, *55*, 328; c) J. Ding, H. Wang, Z. Li, A. Kohandehghan, K. Cui, Z. Xu, B. Zahiri, X. Tan, E. M. Lotfabad, B. C. Olsen, D. Mitlin, *ACS Nano* **2013**, *7*, 11004; d) H. Song, N. Li, H. Cui, C. Wang, *Nano Energy* **2014**, *4*, 81.
[12] a) H. G. Wang, Z. Wu, F. L. Meng, D. L. Ma, X. L. Huang, L. M. Wang, X. B. Zhang, *ChemSusChem* **2013**, *6*, 56; b) W. Luo, J. Schardt, C. Bommier, B. Wang, J. Razink, J. Simonsen, X. Ji, *J. Mater. Chem. A* **2013**, *1*, 10662; c) L. Fu, K. Tang, K. Song, P. A. Van Aken, Y. Yu, J. Maier, *Nanoscale* **2014**, *6*, 1384; d)T. Chen, Y. Liu, L. Pan, T. Lu, Y. Yao, Z. Sun, D. H. C. Chua, Q. Chen, J. Mater. Chem. A, 2014, 2, 4117; e) W. Li, L. Zeng, Z. Yang, L. Gu, J. Wang, X. Liu, J. Cheng, Y. Yu, *Nanoscale* **2014**, *6*, 693; f)Y. Liu, F. Fan, J. Wang, Y. Liu, H. Chen, K. L. Jungjohann, Y. Xu, Y. Zhu, D. Bigio, T. Zhu, C. Wang, *Nano Lett.* **2014**, *14*, 3445.
[13] Y. L. Cao, L. F. Xiao, M. L. Sushko, W. Wang, B. Schwenzer, J. Xiao, Z. M. Nie, L. V. Saraf, Z. G. Yang, J. Liu, *Nano Lett.* **2012**, *12*, 3783.
[14] a) Y.-X. Wang, S.-L. Chou, H.-K. Liu, S.-X. Dou, *Carbon* **2013**, *57*, 202; b)Y. Yan, Y.-X. Yin, Y.-G. Guo, L.-J. Wan, Adv. Energy Mater. 2014, 4, 1301584.
[15] J. P. Paraknowitsch, A. Thomas, *Energy Environ. Sci.* **2013**, *6*, 2839.
[16] a) Z. S. Wu, W. C. Ren, L. Xu, F. Li, H. M. Cheng, *ACS Nano* **2011**; b) L. Qie, W. M. Chen, Z. H. Wang, Q. G. Shao, X. Li, L. X. Yuan, X. L. Hu, W. X. Zhang, Y. H. Huang, *Adv. Mater.* **2012**, *24*, 2047; c) A. L. M. Reddy, A. Srivastava, S. R. Gowda, H. Gullapalli, M. Dubey, P. M. Ajayan, *ACS Nano* **2010**, *4*, 6337; d) X. F. Li, D. S. Geng, Y. Zhang, X. B. Meng, R. Y. Li, X. L. Sun, *Electrochem. Commun.* **2011**, *13*, 822; e) Z. Li, Z. W. Xu, X. H. Tan, H. L. Wang, C. M. B. Holt, T. Stephenson, B. C. Olsen, D. Mitlin, *Energy Environ. Sci.* **2013**, *6*, 871; f) Y. Mao, H. Duan, B. Xu, L. Zhang, Y. S. Hu, C. C. Zhao, Z. X. Wang, L. Q. Chen, Y. S. Yang, *Energy Environ. Sci.* **2012**, *5*, 7950.
[17] Y. H. Xue, J. Liu, H. Chen, R. G. Wang, D. Q. Li, J. Qu, L. M. Dai, *Angew. Chem. Int. Ed.* **2012**, *51*, 12124.
[18] F. Du, D. Yu, L. Dai, S. Ganguli, V. Varshney, A. Roy, *Chem. Mater.* **2011**, *23*, 4810.
[19] a) Y. Xue, D. Yu, L. Dai, R. Wang, D. Li, A. Roy, F. Lu, H. Chen, Y. Liu, J. Qu, *Phys. Chem. Chem. Phys.* **2013**, *15*, 12220; b) S. Wang,

E. Iyyamperumal, A. Roy, Y. Xue, D. Yu, L. Dai, *Angew. Chem., Int. Ed.* **2011**, *50*, 11756.
[20] a) D. T. Welna, L. Qu, B. E. Taylor, L. Dai, M. F. Durstock, *J. Power Sources* **2011**, *196*, 1455; b) W. Lu, A. Goering, L. Qu, L. Dai, *Phys. Chem. Chem. Phys.* **2012**, *14*, 12099.
[21] J. D. Roy-Mayhew, D. J. Bozym, C. Punckt, I. A. Aksay, *ACS Nano* **2010**, *4*, 6203.
[22] I. K. Moon, J. Lee, R. S. Ruoff, H. Lee, *Nat. Commun.* **2010**, *1*, 73.
[23] a) F. Zhang, T. Zhang, X. Yang, L. Zhang, K. Leng, Y. Huang, Y. Chen, *Energy Environ. Sci.* **2013**, *6*, 1623; b) B. Kumar, M. Asadi, D. Pisasale, S. Sinha-Ray, B. A. Rosen, R. Haasch, J. Abiade, A. L. Yarin, A. Salehi-Khojin, *Nat. Commun.* **2013**, *4*, 2819.
[24] I.-Y. Jeon, D. Yu, S.-Y. Bae, H.-J. Choi, D. W. Chang, L. Dai, J.-B. Baek, *Chem. Mater.* **2011**, *23*, 3987.